Bio-Design and Manufacturing (2022) 5:465–480
https://doi.org/10.1007/s42242-022-00198-z

RESEARCH ARTICLE

A 3D in vitro co-culture model for evaluating biomaterial-mediated modulation of foreign-body responses

Betul Cakmak[1] · Pelin Saglam-Metiner[1] · Goze Beceren[1] · Yu S. Zhang[2] · Ozlem Yesil-Celiktas[1]

Received: 4 December 2021 / Accepted: 23 March 2022 / Published online: 18 May 2022

Abstract

The immune response after implantation of a biomaterial may shorten the functional life of the implant, depending on the degree of the response. In this study, we used a polyacrylamide-alginate (PAAm-Alg) hydrogel, which has been previously characterized as a biocompatible material and shown to enhance regeneration of cartilage in vivo, along with a graphite-enhanced hydrogel (PAAm-Alg-G) as a non-biocompatible counterpart, to evaluate macrophage attachment and polarization to pro- or anti-inflammatory phenotypes. The performance of each biomaterial in the presence of fibroblasts and chondrocytes was validated by an in vitro model which demonstrated modulation of the foreign-body response. A blend of 5% gelatin methacryloyl and 0.1% methacrylated hyaluronic acid was optimized to mimic the extracellular matrix (ECM) and support cell viability, proliferation, migration, and functionality at an initial concentration of 3.25×10^5 cells/mL. The PAAm-Alg-G hydrogel localized in the simulated ECM showed cytotoxic and genotoxic effects for both fibroblasts and chondrocytes, while exhibiting a proliferative effect on macrophages with elevated immune response. The M1/M2 ratio was 0.73 for PAAm-Alg hydrogel but 2.64 for PAAm-Alg-G, leading to significant M1 dominance ($p < 0.0001$), as expected, on day 13. Moreover, loading PAAm-Alg hydrogel with transforming growth factor beta-3 (TGF-β3) resulted in a slightly more balanced M1/M2 ratio of 0.87 ($p > 0.05$). The interleukin-6 (IL-6) concentration secreted in the presence of PAAm-Alg hydrogel (4.58 pg/mL) significantly decreased ($p < 0.0001$) on day 13, while the increase ($p < 0.0001$) in interleukin-10 (IL-10) concentration (120.73 pg/mL) confirmed the switch from a pro-inflammatory to an anti-inflammatory response. Predicting immune responses by developing a simplistic yet powerful three-dimensional in vitro model provides advantages in preparing for clinical use of biomaterials.

Graphic abstract

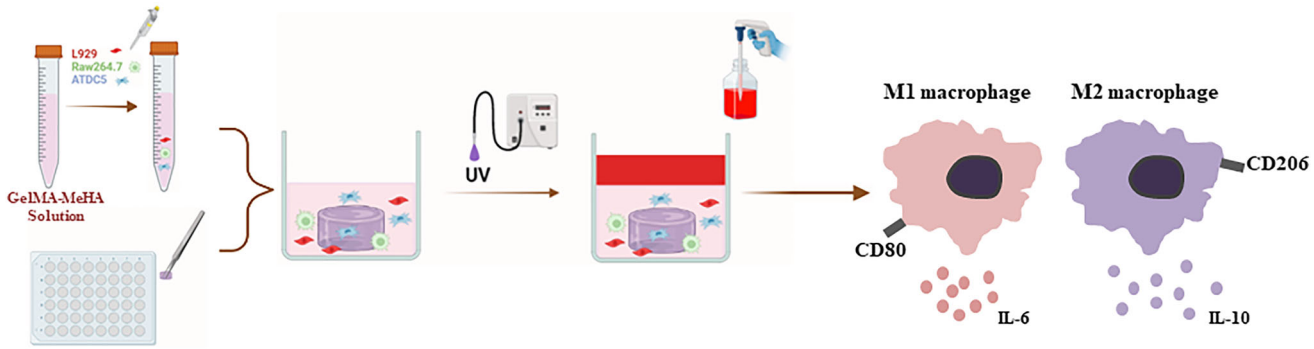

Keywords Biomaterial · Macrophage polarization · Genotoxicity · Biocompatibility · Immune response

✉ Ozlem Yesil-Celiktas
ozlem.yesil.celiktas@ege.edu.tr

[1] Department of Bioengineering, Faculty of Engineering, Ege University, 35100 Izmir, Turkey

[2] Division of Engineering in Medicine, Brigham and Women's Hospital, Department of Medicine, Harvard Medical School, Cambridge, MA, USA

Introduction

The utilization of biomaterials to improve the physiological function of diseased or damaged tissues through replacement or regeneration is imperative in many fields such as tissue engineering, drug delivery, and medical implantation [1]. Implantable biomaterials vary functionally based on the specific application and care is taken in designing materials that meet the desired requirements, due to the complex nature of the human body [2]. In addition, biocompatibility is of the utmost importance when ensuring that no negative reactions are triggered in the body when a biomaterial is implanted [3]. Polymeric hydrogels are among the most preferred implantable biomaterials in many applications such as heart valves, vascular grafts, hip/knee joints, menisci, and tendons/ligaments [4]. Hydrogels, which can absorb large amounts of water and biological fluids, mimic natural living tissues more than many other biomaterials due to their high water content, porosity, soft structure, and stability [5]. Despite the significant progress in understanding and using hydrogels, problems can still be encountered with the immune system during and after implantation [6]. The interaction of the biomaterial with the host environment begins soon after implantation and is generally recognized as foreign by the immune system [7]; immunological responses are triggered and the periphery of the biomaterial is covered with serum proteins, mucosal secretions, microbiota, and extracellular fluids [8]. With this coating, the biomaterial surface becomes susceptible to microbial and cellular adhesions, and macrophages, fibroblasts, and foreign-body giant cells attempt to phagocytize the biomaterial to isolate it from the host tissue [9]. Activation of the defense mechanism may cause excessive responses that may in turn, undesirably damage the host tissues. Macrophages can be phenotypically polarized by the microenvironmental stimuli surrounding them. Depending on the duration and severity of the immune response developed by macrophages against the post-implantation biomaterial, it can either cause tissue repair and regeneration or tissue damage and fibrosis. The first step of the immune response is characterized by recruitment of pro-inflammatory macrophages to the tissue–biomaterial interface [10]. Notably, recent studies have shown that macrophages, which have significant plasticity and distinct functional groups, may be induced dynamically into the classically activated pro-inflammatory (M1) or alternatively activated anti-inflammatory (M2) phenotypes due to their profiles (i.e., phagocytosis and cytokine release) [11]. For instance, M1 macrophages, with their highly phagocytic nature and ability to produce surface markers (i.e., C–C chemokine receptor type 7 and cluster of differentiation 80 (CD80)) as well as pro-inflammatory cytokines (interleukin (IL)-1β, IL-6, and tumor necrosis factor (TNF)-α), maintain early innate damage responses [12]. In contrast, M2 macrophages, which have a reparative function in late-stage resolution of inflammation and repairment, secrete anti-inflammatory cytokines (i.e., IL-1RA, IL-10, transforming growth factor (TGF)-β1) along with surface markers (i.e., CD163 and CD206) [13]. Overall, both M1- and M2-type macrophages play a role in regulating inflammation in response to implantable biomaterials [14]. Polarization to the M1 or M2 phenotype is a key mechanism in the tissue-healing process and is important for the selection of biomaterials. Therefore, predetermination and control of immune responses against biomaterials is of paramount importance in biomaterial design [15].

However, the lack of suitable methods for conducting a comprehensive risk assessment of implantable biomaterials results in failures in clinical application. Recently, pre-implantation of diagnostic technologies has been studied with the aim of selecting the most suitable biomaterials for potential implantable devices. The findings should lead to a significant improvement in risk assessment and reduce post-implantation complications [16]. Researchers have focused on developing methods to monitor, measure, and control the immune response activated by macrophages subsequent to implantation. For instance, an in vitro assay characterizing the dynamic inflammatory response of human monocyte-derived macrophages to biomaterials was developed and coupled with quasi-mechanistic analysis in silico [17]. The major emphasis has been on determination of the host's immune response to the implanted biomaterial prior to implantation and development of methods to understand how this response can be utilized to design and fabricate successful implantable biomaterials [18]. Various in vivo and in vitro models have been developed to investigate the immune response to biomaterials [19, 20]. In vitro models, which have been widely used for determination of immune response, were created by seeding immune cells on the surface of biomaterials [21–23]; this limited recapitulation of host-biomaterial interactions [24]. Alternatively, three-dimensional (3D) models have been adopted that better mimicked in vivo conditions with respect to fundamental biological properties of cells such as viability, morphology, proliferation, differentiation, response to stimuli, gene expression, and cell–cell and cell–extracellular matrix communication [25]. As the immune response against biomaterials in the tissues occurs in a spatiotemporal manner, working with an effective in vitro 3D model can provide physiologically relevant results. In this study, we developed an in vitro 3D model to determine the immune response to implantable hydrogel-based biomaterials that can be used in cartilage-damage repair. The model was designed to assess specific biological mechanisms of host response with particular emphasis on cytotoxicity, genotoxicity, cell proliferation, cytokine release, and macrophage polarization. We also used two hydrogels to validate our in vitro model; one of them was

a biocompatible polyacrylamide-alginate hydrogel (PAAm-Alg), whereas a graphite-enhanced version (PAAm-Alg-G) was deliberately included to introduce a non-biocompatible hydrogel to the model.

Experimental methods

Materials

We purchased gelatin from porcine skin (G2500-500G), methacrylic anhydride (276,685), 2-hydroxy-4'-(2-hydroxyethoxy)-2-methylpropiophenone (Irgacure2959) (410,896-10G), Dulbecco's modified Eagle's medium–high glucose (D6546), DMEM-F12 (D6421), RPMI-1640 (R8758), dialysis tubing cellulose membrane (D965), lipopolysaccharide (LPS) from *Escherichia coli* O111:B4 (L2630-10MG), 3-(4,5-dimethylthiazol-2-yl)-2,5-diphenyl tetrazolium bromide (MTT) (M5655-5X1G), Hoechst 33,258 (B2883), and 4,6-diamidino-2-phenylindole (DAPI) (D9542) from Sigma-Aldrich (Dorset, UK). We purchased anti-CD80 antibody [16-10A1](ab106162), anti-mannose receptor antibody [15–2](ab8918), Alexa Fluor 488 conjugated-goat anti-armenian hamster IgG H&L antibody (ab173003), Alexa Fluor 594 conjugated-goat anti-mouse IgG H&L antibody (ab150116), and hyaluronic acid sodium salt (HA) (ab143634) from Abcam (Massachusetts, USA. A LEGEND MAX™ mouse IL-6 ELISA kit (431,307) and LEGEND MAX™ mouse IL-10 ELISA kit (431,417) were purchased from Biolegend (California, USA). Red CellTracker™ CMTPX (C34552) and green CellTracker™ CMFDA (C7025) were purchased from Thermo Fisher Scientific (Massachusetts, USA). TGF-β3 (Human CellExp™ TGF-β3) was purchased from Biovision (California, USA), PBS (phosphate buffer saline) Ca^{2+}-/Mg^{2+}-free (L1825) was purchased from Merck (Darmstadt, Germany); collagenase (17,018–029) from Gibco (Newyork, USA); an OxiSelect™ Comet Assay Kit (3-Well Slides) (STA-351) from Cell Biolabs (Massachusetts, USA); and a Live/Dead® kit (L3224) from Invitrogen (Massachusetts, USA).

Synthesis of gelatin methacryloyl (GelMA) and methacrylated hyaluronic acid (MeHA)

GelMA and MeHA were synthesized as the first step in developing the in vitro 3D model. For GelMA synthesis, we dissolved 10 g of type A gelatin from porcine skin in 100-mL PBS at 50 °C; 8 mL of methacrylic anhydride was added dropwise and stirred for 3 h at 50 °C. The GelMA solution was diluted with 100 mL of PBS preheated to 50 °C to stop the reaction and dialyzed using 12–14 kDa cutoff dialysis membranes (MWCO 12–14.000) to remove the toxic unreacted molecules at 40 °C for at least 5 days in distilled water. Then, the purified solution was diluted with 200 mL of ultrapure water, and the pH was adjusted to 7.4 using sodium bicarbonate ($NaHCO_3$). The solution was filtered using a vacuum filtration cup with 0.22-μm pores (Millipore), frozen at –80 °C, and lyophilized. For MeHA synthesis, 100 mg of hyaluronic acid sodium salt was dissolved in 30 mL of ultrapure water at room temperature (RT) overnight and 750 μL of methacrylic anhydride was added dropwise. The reaction was carried out at 4 °C overnight by maintaining the pH between 8 and 9. After a fourfold dilution with ultrapure water, the MeHA solution was dialyzed using 12–14 kDa cutoff dialysis membranes at 4 °C for at 3 days in distilled water. The pH was adjusted to 7.4 and lyophilized. Both solutions were stored in the dark at 4 °C.

Characterization of GelMA and MeHA

We scanned the attenuated total reflection Fourier-transform infrared spectroscopy (ATR FTIR) spectra of gelatin, lyophilized GelMA, HA, and lyophilized MeHA with the PerkinElmer Spectrum 100 instrument at wavelengths of 600–4000 cm^{-1}. ATR-FTIR was used to qualitatively evaluate the degree of methacryloyl substitution of the gelatin and hyaluronic acid.

Synthesis of hydrogels and biocompatibility

PAAm-Alg hydrogel containing 14% total polymer was prepared as described in our previous publication [26], while PAAm-Alg-G hydrogel was prepared with the addition of 1.5% graphite. Both were sterilized with ultraviolet (UV) light for 2 h. For TGF-β3-loaded PAAm-Alg hydrogel (PAAm-$Alg_{TGF\text{-}\beta3}$) preparation, we added TGF-β3 to the PAAm-Alg pre-solution simultaneously with the crosslinking agents, resulting in a final concentration of 15 ng of TGF-β3 per 0.55 g of hydrogel. In order to evaluate the biocompatibility of hydrogels, we performed MTT and agar diffusion tests to assess cytotoxicity. We used the Comet assay, also known as single-cell gel electrophoresis, to provide data on genotoxicity.

Cytotoxicity

In accordance with "ISO 10993–12: Sample preparation and reference materials" standards [27], we transferred the hydrogels into sterile 50-mL falcon tubes at the recommended ratio of hydrogel surface area/medium volume (3 cm^2/mL) and incubated them in DMEM F12 medium containing 0.1% gentamicin and 1% sodium bicarbonate at 37 °C with 5% CO_2 for 72 h to produce conditioned hydrogel extracts. Based on *ISO 10993–5: Tests for* in vitro*cytotoxicity standards* (ISO 10993–5:2012), we performed an MTT assay to evaluate the effects of PAAm-Alg and PAAm-Alg-G hydrogel

extracts on the cell viability of chondrogenic cells derived from mouse teratocarcinoma cells (ATDC5), mouse connective tissue fibroblasts (L929), and mouse macrophages (Raw264.7) (ATCC, Virginia, USA). Cells were seeded in 96-well plates (1×10^4 cells/well) and incubated overnight at 37 °C and 5% CO_2. Subsequently, the medium was removed and hydrogel extract diluted in the fresh medium at ratios of 1, 1/2, 1/4, 1/8, or 1/16 was added at to each well (100 μL). Cells treated with only growth medium and cells treated with dimethyl sulfoxide (DMSO) were considered to be the positive and negative controls, respectively. After 24, 48, and 72 h of incubation, supernatants were removed, 10% MTT solution (diluted in medium from 5 mg/mL of stock solution, M5655, Sigma-Aldrich) was added to each well (100 μL), and the wells were incubated for 3 h at 37 °C. Then, MTT was removed and DMSO was added to each well. We measured the absorbance with a microplate reader at 570 nm (BioTek, Korea) and calculated cell viability (%) with GraphPad Prism 8.3.0.

An agar diffusion test was also performed as an indirect contact test, in accordance with *ISO 10993–5: Tests for* in vitro*cytotoxicity standards*. For this test, ATDC5 and L929 cells were seeded in 6-well plates (3×10^5 cells/well). When 80%–90% occupancy was achieved, the medium was removed and replaced with agar medium (3 mL/well). The agar medium was prepared by mixing autoclaved sterile 1% low-melting-point agar and DMEM F12 medium containing 5% FBS and %1 $NaHCO_3$ at a ratio of 50:50 at 35–37 °C. Once the agar medium solidified, we placed sterile hydrogels in the middle of the agar surface and incubated them for 72 h at 37 °C. After incubation, the hydrogel and agar were carefully removed and Live/Dead® staining was performed. A solution of 2-μM calcein acetoxymethyl ester (Calcein AM) and 4-μM ethidium homodimer-1 (EthD-1) prepared in PBS was applied directly to the cells at 1 mL/well and incubated for 45 min at room temperature in the dark. Excess dye was then washed off with PBS and the cells were visualized with fluorescence microscopy (Zeiss, Axio Vert.A1, Germany).

Genotoxicity

We performed an alkaline comet assay to evaluate the potential DNA damage induced by the PAAm-Alg and PAAm-Alg-G hydrogels, with the OxiSelect™ Comet Assay Kit (STA-351, Cell Biolabs). Briefly, ATDC5, L929, and Raw264.7 cells were seeded onto 24-well plates at a density of 3×10^5 cells/well and incubated overnight. Cells were treated with a 1/1 concentration of hydrogel extract/growth medium as positive control and H_2O_2/Mitomycin C (MitC) as negative control. After 72 h of incubation, live cells were removed from the culture plate by trypsinization and centrifuged 2 times in PBS. The low-gelling-temperature agarose (1% w/v) and the cell suspension (10^5 cells/mL) were mixed at a ratio of 10:1 at 37 °C, then 80 μL of the mixture was spread well over each OxiSelect™ Comet slide. The slides were kept on a metal tray on ice at 4 °C for 15 min to allow agarose gelation. After that, the slides (in the slide carrier apparatus) were incubated in 250 mL of alkaline lysis buffer solution (pH:10) for 2 h at 4 °C and in alkaline solution for 30 min at 4 °C. Then, the cell-agarose-laden slides were placed in a COMPAC-50 electrophoresis tank filled with fresh alkaline electrophoresis solution, and electrophoresis was carried out in constant mode, programmed at 21 V and 700 mA for 30 min. After electrophoresis, the slides were neutralized in distilled water 3 times each for 2 min at 4 °C, and washed in 70% EtOH solution for 5 min. About 100 μL of Vista Green fluorescent dye (prepared in TE buffer solution at a rate of 1/10,000) was added to each well of the dried slides and incubated for 20 min at RT. Finally, we visualized cell nuclei under a fluorescence microscope (Zeiss, Axio Vert.A1, Germany) with a 40 × objective magnification and performed comet analysis in the ImageJ program with 20 cells per sample. The percentages of DNA in the comet tail and the olive tail moment (OTM) were used as a measure of the amount of DNA damage, and were analyzed in GraphPad Prism 8.3.0.

Fabrication and optimization of in vitro 3D model with GelMA-MeHA

To assess the immune response induced by hydrogels, we developed an in vitro 3D model with GelMA-MeHA recapitulating the ECM. First, hydrogel PAAm-Alg or PAAm-Alg-G was placed into 48-well plates. ATDC5, L929, and Raw264.7 cells were trypsinized and counted, and these three cell types were resuspended together in sterile GelMA-MeHA prepolymer solution at concentrations of 1.5×10^5, 1.5×10^5, and 0.25×10^5 cells/mL, respectively. Subsequently, 700 μL of the solution-cell mixture was transferred to the well to completely cover the hydrogels previously placed and photopolymerized using UV light (Omnicure S2000, Lumen Dynamics, Canada) at 800 mW, 8 cm, and 30 s to form the in vitro 3D GelMA-MeHA model, in which three types of cell-loaded GelMA-MeHA matrices were placed around the PAAm-Alg or PAAm-Alg-G hydrogels. The cells were homogeneously suspended around the hydrogels in the matrix. With regard to the experimental set, LPS-free medium or 1 μg/mL of LPS-containing medium was added to the photocrosslinked 3D GelMA-MeHA model. Then, the 3D model was incubated at 37 °C and 5% CO_2 for up to 13 days and the original cell culture medium was replaced every other day. The viability, migration, and immune response of the cells were assessed at predetermined time points (days 1, 4, 7, 10, and 13).

To optimize the 3D model, we evaluated different GelMA concentrations (5%, 10%, 15% w/v) and different total cell

concentrations (1.625×10^5 cells/mL, 3.25×10^5 cells/mL, 6.5×10^5 cells/mL), as well as inclusion of HA (0.1% w/v) in GelMA (5% w/v) with Live/Dead® analysis.

Immune response induced by hydrogels

Assessment of cell viability

The PAAm-Alg and PAAm-Alg-G hydrogels were loaded into the matrix and the effects on cell viability were assessed at predetermined time points using a LIVE/DEAD™ viability/cytotoxicity assay kit in the 3D GelMA-MeHA in vitro model. After removing the medium, we washed each well with PBS (1X) 3 times and stained it with Calcein AM (2 μM) and EthD-1 (4 μM) for 90 min at 37 °C. Excess dye was then washed 3 times with PBS and cells were observed with fluorescence microscopy (Zeiss, Axio Vert.A1).

Tracking of cell proliferation

To evaluate time-lapse cell proliferation around hydrogels in the 3D GelMA-MeHA in vitro model, we stained L929, Raw 264.7, and ATDC5 cells with three differently colored fluorescent dyes, respectively: Red CellTracker™ CMTPX (15 μM), Green CellTracker™ CMFDA (25 μM), and Hoechst 33,258 (15 μM). Staining was carried out for 45 min at 37 °C with 5% CO_2. We then added the cells to the GelMA-MeHA solution. The labeled cells were imaged with fluorescence microscopy (Zeiss, Axio Vert.A1) at predetermined time points. Cell counts were then analyzed with the ImageJ program.

Analyses of cytokines

For pro-inflammatory and anti-inflammatory cytokine analyses, we collected the supernatants from the 3D cultures at predetermined time points. We quantified the IL-6 and IL-10 concentrations in the supernatants using mouse IL-6 and IL-10 ELISA kits, according to the manufacturer's instructions. Data were analyzed with GraphPad Prism 8.3.0.

Assessment of macrophage polarization

To assess M1 and M2 macrophage phenotypes, we performed immunocytochemical analyses at predetermined time points. Cells were harvested individually from the 3D model using collagenase solution (100 U/mL) prepared by dissolving collagenase in PBS (1X) for 1 h at 37 °C, seeding it in a 48-well plate, and incubating it overnight. Next, the cells were fixed with paraformaldehyde (4% w/v) for 30 min at 4 °C and permeabilized with Triton X-100 (0.1% v/v) for 15 min at RT. For blocking, the cells were incubated in bovine serum albumin (BSA) (1% w/v) solution in PBS (1X) at RT for 1 h and incubated overnight at 4 °C with anti-CD80 (Armenian hamster monoclonal antibody, 1:80 dilution) and anti-mannose receptor CD206 (mouse monoclonal antibody, 1:100 dilution) primary antibodies (M1 and M2 markers) in Tris-buffered saline containing Triton X-100 (0.025% v/v) and BSA (3% w/v). On the following day, the cells were washed with PBS (1X) and incubated with Alexa Fluor 488 conjugated-goat anti-Armenian hamster (1:200 dilution) and Alexa Fluor 594 conjugated-goat anti-mouse (1:200 dilution) secondary antibodies (for CD80 and CD206, respectively) for 1 h at RT. Subsequently, we stained the nuclei for 15 min using DAPI (1.5 μg/μL) and imaged the cells using microscopy (Zeiss, Axio Vert.A1, Germany). We used ImageJ to quantify CD80 and CD206 and then calculated the M1/M2 expression ratios.

Statistical analyses

Comet assay data were statistically analyzed with one-way analysis of variance (ANOVA), followed by Dunnett's multiple comparison test; the ELISA results were analyzed with two-way ANOVA, followed by Tukey's multiple comparison test in GraphPad Prism 8.3.0 program, considering $p < 0.05$ as statistically significant with a ± 95% confidence interval. Data are presented as the means ± standard errors for the comet assay ($n = 20$), while data are presented as the means ± standard deviations for analyses of cytokines ($n = 2$). To indicate degree of significance, ns: $p > 0.05$, *: $p < 0.05$, **: $p < 0.01$, ***: $p < 0.001$, ****: $p < 0.0001$ were used.

Results and discussion

Synthesis and characterization of GelMA and MeHA

GelMA and MeHA were synthesized, to mimic the natural ECM and support the viability and functionality of cells. The reaction of gelatin and hyaluronic acid with methacrylic anhydride was confirmed with FTIR. GelMA is a semi-synthetic polymer formed by the addition of methacryloyl groups to the amine-containing side groups of gelatin [28]. The amide bands of GelMA show different vibrational states of the peptide bond. The FTIR result of GelMA with peaks at 1243, 1540, 1645, 3063, and 3295 cm^{-1} is shown in Fig. S1a (Supplementary Information). Compared to pure gelatin, the overall FTIR spectrum of GelMA exhibited a shift toward higher wavelengths as a feature of methacryloyl reactions. The amino group of gelatin was converted to the amide group in GelMA. The FTIR results obtained are consistent with the literature and show that GelMA was successfully synthesized [29]. HA containing primary hydroxyl groups was

reacted with methacrylic anhydride to add methacrylate pendant groups. The FTIR spectra of MeHA and HA are shown in Fig. S1b. The family of vibrational bands extending from 1450 to 1700 cm^{-1} results from the overlap of the amide peaks with the carboxylate stretch bands of HA. A weak band appeared due to carbon–hydrogen (C-H) stretching around 2922 cm^{-1}. A broad infrared signal observed around 3000–3600 cm^{-1} was defined as a stretching peak due to the oxygen-hydrogen (O–H) and nitrogen–hydrogen (N–H) groups involved in hydrogen bonding. C–O–C stretching was confirmed by the peaks found at 667 and 1028 cm^{-1}. MeHA showed new peaks attributable to the C = O groups added at 1731 cm^{-1} and the C = C groups added at 1643 cm^{-1}. Other characteristic FTIR peaks of HA in the formation of MeHA were preserved after the reaction. FTIR results showed that the sodium salt of hyaluronic acid reacted with methacrylic anhydride [30, 31].

Preparation of hydrogels and biocompatibility assays

Our idea was to investigate the interaction between the host environment and both a biocompatible and a non-biocompatible material in order to determine the accuracy and consistency of the 3D co-culture model. PAAm-Alg hydrogel was used as a biocompatible material, and was synthesized and fully characterized in our previous study [26]. Meanwhile, to achieve non-biocompatiblity, we added 1.5% graphite to PAAm-Alg, thus creating PAAm-Alg-G hydrogel. We performed MTT, agar diffusion, and comet assays to assess cytotoxicity and genotoxicity. For the MTT assay, different dilution ratios (1, 1/2, 1/4, 1/8, 1/16 v/v) of hydrogel extracts were prepared with the growth medium to determine cytotoxicity on L929, ATDC5, and Raw264.7 cells at 72 h. The extraction medium needed to be diluted to protect cells against osmotic shock caused by substances released into the culture medium and provide in vivo-like conditions, in which these substances could be tolerated by the body's circulatory system [32]. In our previous study, we showed with MTT and agar diffusion assays at 72 h that PAAm-Alg hydrogels exerted no cytotoxic effect on L929 or ATDC5 cells [19]. Nevertheless, in this study, the presence of graphite in the PAAm-Alg-G hydrogels resulted in a cytotoxic effect for both L929 (1 and 1/2 ratios of extract) and ATDC5 (1, 1/2, and 1/4 ratios of extract) cells (< 70% cell viability), while leading to proliferation of Raw264.7 cells (≥ 100% cell viability for 1/4, 1/8, and 1/16 ratios of extract) at 72 h (Fig. S2a). Liu et al. reported that implanted graphite films could not integrate with new bone tissue even after four weeks because cell viability and adhesion were not supported; these processes normally benefit from cell proliferation and osteogenic differentiation [33]. Furthermore, Live/Dead® images of an agar diffusion test qualitatively supported the cytotoxicity of PAAm-Alg-G hydrogels against L929 and ATDC5 cells, compared to a positive control group at 72 h (Fig. S2b). The agar layer was used as a barrier and the potential indirect toxic effects of substances leached from hydrogels were determined [34].

In addition, we evaluated the genotoxicity of PAAm-Alg and PAAm-Alg-G hydrogels on L929, ATDC5, and Raw264.7 cells by comet assay (also known as single-cell gel electrophoresis assay) at 72 h (Fig. 1). Comet assay is a rapid, efficient, and highly sensitive fluorescence microscopic method used for the detection of potential DNA damage at the cellular level [35]. In the comet structure, the intact DNA is termed the "head" and the damaged DNA trace is termed the "tail." DNA damage is determined by measuring the displacement between the head and the resulting tail. The ratio of the amount of DNA in the tail to the head region is proportional to the initial DNA damage, and damaged DNA migrates more than intact DNA, producing a "comet tail" shape. The "olive tail moment" and "DNA in the comet tail (%)" are the two most common parameters for analyzing comet test results. The olive tail moment is an appropriate index of induced DNA damage, taking into consideration both the migration of genetic material and the relative amount of DNA in the tail [36]. When the comet images were examined, we did not observe tail formation in the positive control group, which is treated only with the growth medium. As expected, we saw long tail formations in the negative control groups (MitC and H_2O_2 treatment) with prominent genotoxic effects in L929, ATDC5, and Raw264.7 cells. Also, the PAAm-Alg-G hydrogel, which had shown to exert cytotoxic effect on cells, caused more damage to the DNA and a comet tail shape was observed as a result of increased migration of damaged DNA, compared to the PAAm-Alg hydrogel (Fig. 1a).

We then analyzed the comet images with ImageJ, and calculated the olive tail moment and DNA percentage in the comet tails of 20 cell nuclei from each experimental group in GraphPad, which enabled us to perform statistical analyses (Fig. 1b). In the results for DNA in comet tails, the PAAm-Alg hydrogel group showed statistically non-significant differences ($p > 0.05$) for all cell lines, whereas the PAAm-Alg-G- and H_2O_2/MitC-treated negative control groups showed significant differences ($p < 0.0001$ for L929 and ATDC5 cells, $p < 0.01$ for Raw264.7 cells) compared to the non-treated positive control group. In the olive-tail-moment analysis, we detected a genotoxic effect only for PAAm-Alg-G hydrogel. The outcomes supported the cytotoxicity results and showed that DNA damage was closely related to graphite content. In summary, the results of all biocompatibility assays revealed the non-toxicity of PAAm-Alg hydrogel and toxicity of PAAm-Alg-G hydrogel.

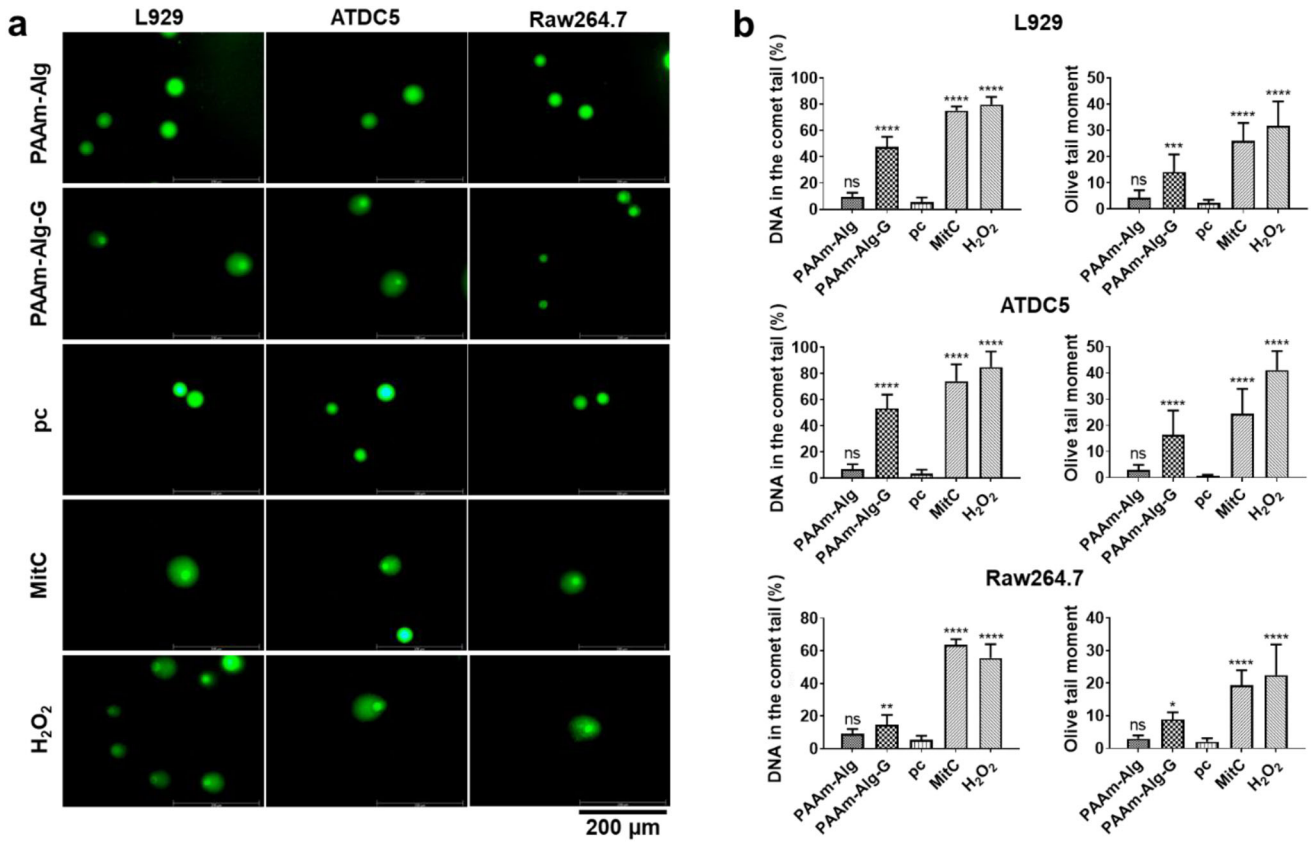

Fig. 1 Comet assay of PAAm-Alg and PAAm-Alg-G hydrogel extracts on L929, ATDC5, and Raw264.7 cells at 72 h (growth medium is pc-positive control and H_2O_2/MitC is negative control). **a** Florescence images and **b** DNA in the comet tail (%) and olive tail moment results. One-way ANOVA, Dunnett's multiple comparison test ns: $p > 0.05$, *$p < 0.05$, **$p < 0.01$, ***$p < 0.001$, ****$p < 0.0001$

Fabrication and optimization of in vitro 3D model with GelMA-MeHA

We used GelMA-MeHA, which provides a good level of ECM mimicry, to create a 3D in vitro model that was physiologically similar to cartilage tissue [37]. We also used chondrocytes in the articular cartilage alongside fibroblasts and macrophage cells in the surrounding synovial tissue (these are known to mediate the immune response) in order to create an immunologically similar cellular microenvironment. Innate immune cells are commonly used to promote post-implantation healing by activating macrophages to generate regenerative cues in the immune response, for example, through macrophage polarization from an inflammatory (M1) phenotype to a reparative/regenerative (M2) phenotype [38]. Fibroblasts are innate immune cells that sense pathogens and harmful molecules in the environment by expressing innate immune receptors such as toll-like receptors, responding by secreting cytokines and chemokines [39]. Chondrocytes, like fibroblasts, participate in the immune response by presenting antigens to macrophages and dendritic cells, indirectly affecting the polarization of macrophages [40]. In order to assess the immune response against biomaterials, it is important that the selected cell lines be able to proliferate, migrate, and perform their functions, supported by high cell viability in a 3D model that mimics the tissue where the biomaterial will be implanted. We found that cells at a concentration of 1.3×10^6 cells/mL in 5%, 10%, and 15% GelMA maintained high cell viability (Fig. S3a). Live/Dead® analyses demonstrated that the developed 3D model created favorable adhesion and a suitable 3D environment for the cells. As the GelMA concentration was increased, cell imaging became unclear, and therefore instead of 10% or 15% GelMA concentrations, we chose a 5% GelMA concentration at which cells could be clearly imaged and monitored. The initial cell concentration was also optimized to allow monitoring of cell proliferation for 13 days. Accordingly, we selected a concentration of 3.25×10^5 cells/mL for development of our 3D model (Fig. S3b). As a next step, we incorporated HA into GelMA hydrogel via UV photopolymerization to increase the specificity of GelMA and generate a tissue-specific 3D biomimetic model, recapitulating in vivo conditions due to the abundance of HA in the articular cartilage and synovial fluid and

contributing to cell proliferation, migration, and morphogenesis [41]. To enrich HA concentration in the 3D model, we added 0.1% (w/v) MeHA, taking into account the preferred HA injection doses for treatment of osteoarthritis [42, 43]. Live/Dead® results showed that the addition of 0.1% MeHA to 5% (w/v) GelMA further promoted cell viability, proliferation, and attachment (Fig. S3c). The GelMA-MeHA in vitro 3D co-culture model provided a conducive adhesion and proliferation environment for cells.

Immune responses induced by various hydrogels

We then evaluated the immune responses to biocompatible (PAAm-Alg) and non-biocompatible (PAAm-Alg-G) hydrogels to be implanted in an inflammatory or healthy environment in the body, using our 3D in vitro GelMA-MeHA model (Fig. 2a).

Assessment of cell viability and proliferation

Cell viability and proliferation were assessed in the absence and presence of LPS, the membrane component of gram-negative bacteria, which creates a pro-inflammatory environment by polarizing macrophages to the M1 phenotype [44]. Using Live/Dead® analyses, we investigated the cytotoxic effects of PAAm-Alg and PAAm-Alg-G hydrogels on L929, ATDC5, and Raw264.7 cells in the 3D culture model in terms of cell viability. In the presence of PAAm-Alg hydrogel and the absence of LPS, the cells exhibited morphologically adherent, large and elongated cell bodies, and easily adapted to the microenvironment by cell–cell interactions and cell proliferation [45] (Fig. 2b). From day 1, the number of dead cells was considerably lower than the number of live cells and the number of viable cells increased continuously over a period of 13 days. At the same time, the cells exhibited homogeneous distribution. In the presence of PAAm-Alg-G hydrogel, cell proliferation was less, more dead cells were observed, and as expected the cells did not show morphological spread (Fig. 2c), due to cytotoxicity and genotoxicity [42].

Cell morphology and proliferation were negatively affected for both hydrogels upon LPS stimulation, yielding morphologically rounded cell bodies with short cell extensions. Less cell proliferation in a pro-inflammatory environment compared to LPS– can be attributed to the fact that LPS stresses the cells by its endotoxic nature as the culture time is prolonged [46]. Overall, the results showed that PAAm-Alg hydrogel exerted no cytotoxic effect, whereas the addition of 1.5% graphite altered cell viability and morphology in the 3D culture model. We also evaluated proliferation of L929, ATDC5, and Raw264.7 cells located in GelMA-MeHA around PAAm-Alg and PAAm-Alg-G hydrogels in the 3D model in both the absence and presence of LPS. Chondrocytes proliferated 2.7-fold less in the presence of PAAm-Alg-G hydrogel than in the presence of PAAm-Alg. (Figs. 3 and S4). Zakrzewska et al. reported that graphite reduced cell viability, proliferation, and adhesion, also arguing that the observed cytotoxic effect of graphite might be due to the presence of highly reactive overhanging carbon bonds on its surface [47].

Interestingly, it has been shown that this effect is cell-type-dependent, and the possible mechanism of toxicity is oxidative stress [48], which causes harmful effects at the cellular level such as cell membrane peroxidation, protein denaturation, and DNA strand breakage [49]. In line with this, chondrocytes, which are shown to undergo the most DNA damage and have the lowest cell viability in the presence of PAAm-Alg-G based on the biocompatibility results of the current study, exhibited less cell proliferation. Fibroblasts (red), macrophages (green), and chondrocytes (blue) were observed to proliferate from day to day in the presence of PAAm-Alg hydrogels, with a homogeneous proliferation pattern (Fig. 3a), whereas cell proliferation of macrophages toward PAAm-Alg-G hydrogels was 1.5-fold higher than toward PAAm-Alg hydrogels (Fig. 3b). Co-proliferation of fibroblasts and macrophages might indicate the phenomenon that prevents integration of the biomaterial after implantation due to delayed tissue healing and fibrous capsule formation [50]. Because of the pro-inflammatory environment induced by LPS, proliferation of macrophages against PAAm-Alg hydrogel was increased by continuous stimulation. The macrophages proliferate and migrate toward the biomaterial under pro-inflammatory conditions by increasing their phagocytic abilities, which enables the removal of cell debris and non-biocompatible biomaterials [51]. Indeed, continuous proliferation of macrophages in LPS + as opposed to LPS– validated the mimicry of the pro-inflammatory environment. In both the presence and absence of LPS in the PAAm-Alg-G group, the cells were mostly clustered around the hydrogel, with higher proliferation of macrophages. In particular, responses in LPS– were similar to responses to the PAAm-Alg hydrogel in LPS + , suggesting a prolonged pro-inflammatory environment created by implantation of a non-biocompatible material such as graphite-enhanced PAAm-Alg [52].

Analysis of cytokines and assessment of macrophage polarization

Since prolonged M1 polarization causes tissue and biomaterial damage due to degradation, and excessive M2 polarization leads to fibrous capsule formation, the use of biomaterials that modulate macrophage polarization toward a more balanced M1/M2 or slightly M2-weighted phenotype is recommended [53]. As expected, in qualitative and quantitative analyses of macrophages (Figs. 4 and S4), the

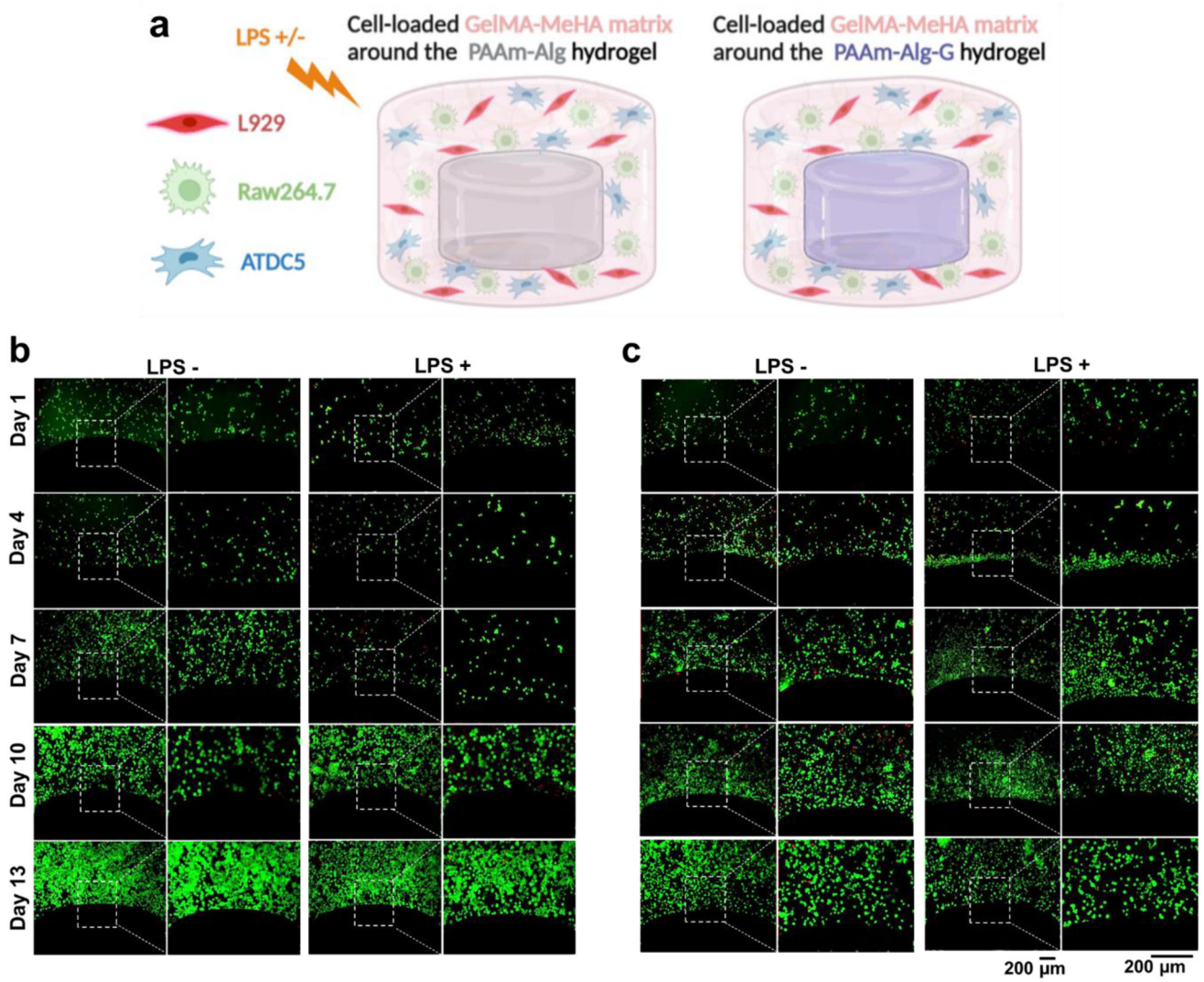

Fig. 2 Evaluation of the effect of hydrogels in the 3D model of cell viability. **a** Schematics depicting PAAm-Alg and PAAm-Alg-G hydrogel-based 3D GelMA-MeHA models. Images of Live and Dead analyses of the 3D model containing **b** PAAm-Alg and **c** PAAm-Alg-G hydrogels. Fluorescent green represents live cells and fluorescent red represents dead cells

M1 profile was predominant (indicated by the M1 surface marker CD80 in green), due to the presence of a continuous pro-inflammatory environment at all times in LPS + in which stained cells surrounded the PAAm-Alg hydrogel (the M1/M2 ratio was significantly dominant on days 7, 10, and 13, $p < 0.0001$). In LPS–, the immune response to trigger wound healing started with the predominance of the M1 profile against the PAAm-Alg hydrogel from day 1 to day 4, whereas the M2 profile (indicated by the M2 surface marker CD206 in red) became significantly more dominant ($p < 0.0001$) on day 7, and then, the M1 and M2 profiles came to a slightly ($p < 0.01$) M2-weighted balance on day 13 with an M1/M2 ratio of 0.73. Incorporation of cytokines and growth factors such as IL-4, IL-10, and TGF-β3 to hydrogels is reported to adjust immune cell functions [54]. In the current study, TGF-β3, known to promote polarization of inflammatory M1 macrophages to reparative M2 macrophages [46], was added to the PAAm-Alg hydrogel. TGF-β3-loaded PAAm-Alg hydrogel (PAAm-Alg$_{TGF\text{-}\beta3}$) led to enhanced activation of the immune response, resulting in numerically higher M1 to M2 polarization (Fig. 4a). M2 proliferation was observed to increase with the presence of PAAm-Alg$_{TGF\text{-}\beta3}$ hydrogels in comparison with PAAm-Alg, resulting in a more balanced M1/M2 ratio closer to 1 at the end of day 10 with an M1/M2 ratio of 0.86 (significant, $p < 0.05$) and day 13 with a ratio of 0.87 (non-significant, $p > 0.05$) (Fig. 4b). The results showed a transition from inflammation to the healing phase, which may be associated with successful repair of damaged tissue and constructive tissue remodeling. Not only the chemical, but also

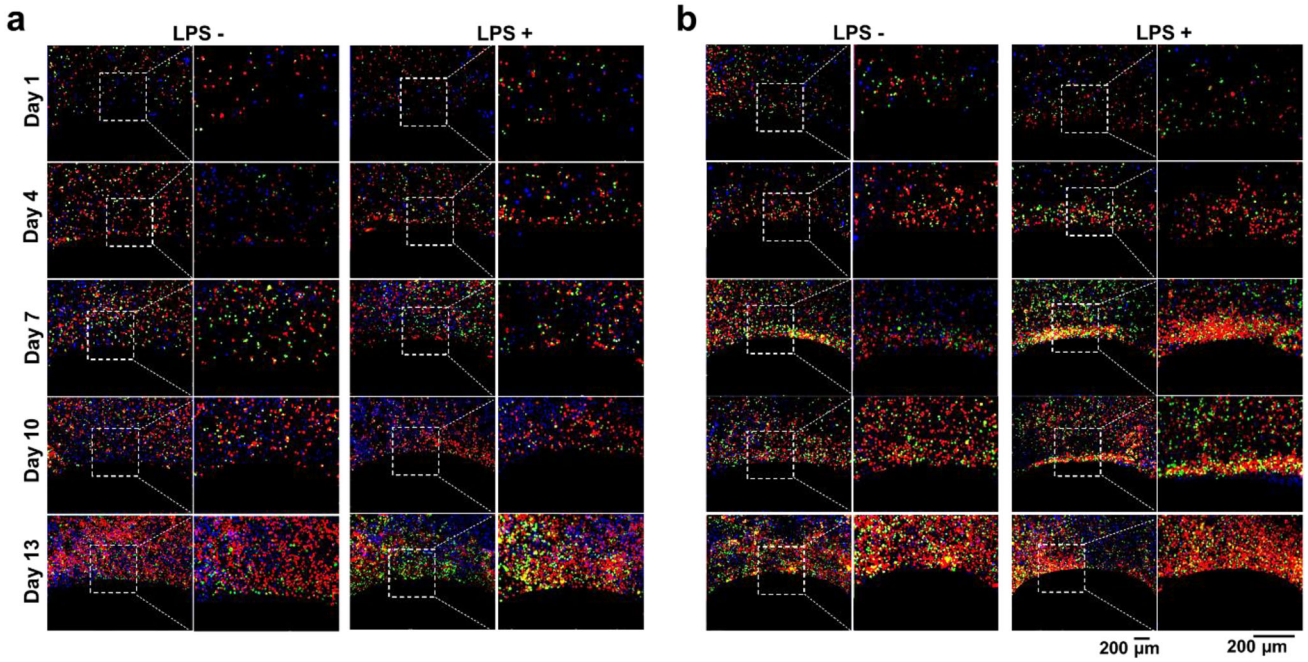

Fig. 3 Evaluation of cell proliferation within the 3D model around **a** PAAm-Al and **b** PAAm-Alg-G hydrogels after CellTracker fluorescent staining. L929 cells are shown in red, Raw264.7 cells in green, and ATDC5 cells in blue

the physical properties of hydrogels, such as stiffness, surface morphology, hydrophobicity, and degradation rate are reported to affect immune response [55]. PAAm-Alg hydrogel has a compression modulus of 38.81 ± 2.1 kPa. Sridharan et al. reported that hydrogels of different stiffnesses with low compressive moduli in the range of 11 and 88 kPa, yield a reduced pro-inflammatory response as opposed to a compressive modulus of 323 kPa [56].

Another interesting factor is that a higher anti-inflammatory response is reported to occur when the surface of polymer-based materials is hydrophobic [57]. Indeed, PAAm-Alg hydrogel is hydrophobic, and the hydrophobicity is increased by loading TGF-β3 [26]. On the other hand, the addition of graphite to PAAm-Alg hydrogel caused consistent M1 polarization; the M1/M2 ratio was always greater than 1.4 and significantly dominant on days 7, 10, and 13, $p < 0.0001$. This is similar to the case of LPS + , where the M1/M2 ratio was significantly dominant on days 4 ($p < 0.0001$), 7 ($p < 0.0001$), 10 ($p < 0.0001$), and 13 ($p < 0.05$). Consistent with our results, Cerqueira et al. showed that non-biocompatible biomaterials increased M1 polarization, while M2 polarization did not changed much [58]. In addition, in various non-healing conditions such as chronic wounds, insufficiently activated pro-inflammatory M1 macrophages have not been observed to be polarized to a reparative M2 phenotype, and thus the likely key mechanism in the tissue healing process is the M1 to M2 phenotypic transition [59]. Long-term polarization of M1 in which polarization to M2 fails indicates the presence of chronic inflammation, which in turn damages the native host tissue and prevents constructive tissue regeneration [60].

We quantitatively determined the release of pro-inflammatory cytokine IL-6 and anti-inflammatory cytokine IL-10 in the 3D model. The inflammatory response was promoted by secretion of IL-6 pro-inflammatory cytokines from the cells from day 1 (11.67 pg/mL) to day 7 (18.12 pg/mL) against PAAm-Alg hydrogels in LPS– (Fig. 5a), and we initiated the cascade required for the healing phase [61]. The pro-inflammatory phase is known to begin immediately after the wound is formed and usually lasts one week [62]. After this period, macrophages polarize from a destructive inflammatory M1 phenotype to a constitutive regenerative M2 phenotype [38]. As M1 macrophages are polarized to M2 macrophages with the release of profibrotic factors, the IL-6 level decreases and the IL-10 level increases [63], a phenomenon which was also observed in the 3D model when the responses to PAAm-Alg and PAAm-$Alg_{TGF\text{-}\beta3}$ hydrogels were assessed. Incorporation of TGF-β3 resulted in more cytokine expressions in the microenvironment due to both macrophage and chondrocyte proliferation; the cytokine concentrations around PAAm-$Alg_{TGF\text{-}\beta3}$ hydrogels were much higher compared to those around hydrogels under both healthy conditions (15-fold more on day 13) and inflammatory conditions (threefold more on day 13). TGF-β isoforms are pleiotropic cytokines found in the bone-cartilage matrix and are involved in a variety of biological functions including cell proliferation, migration, and differentiation; and fibrosis, tissue homeostasis, and immune response, with both

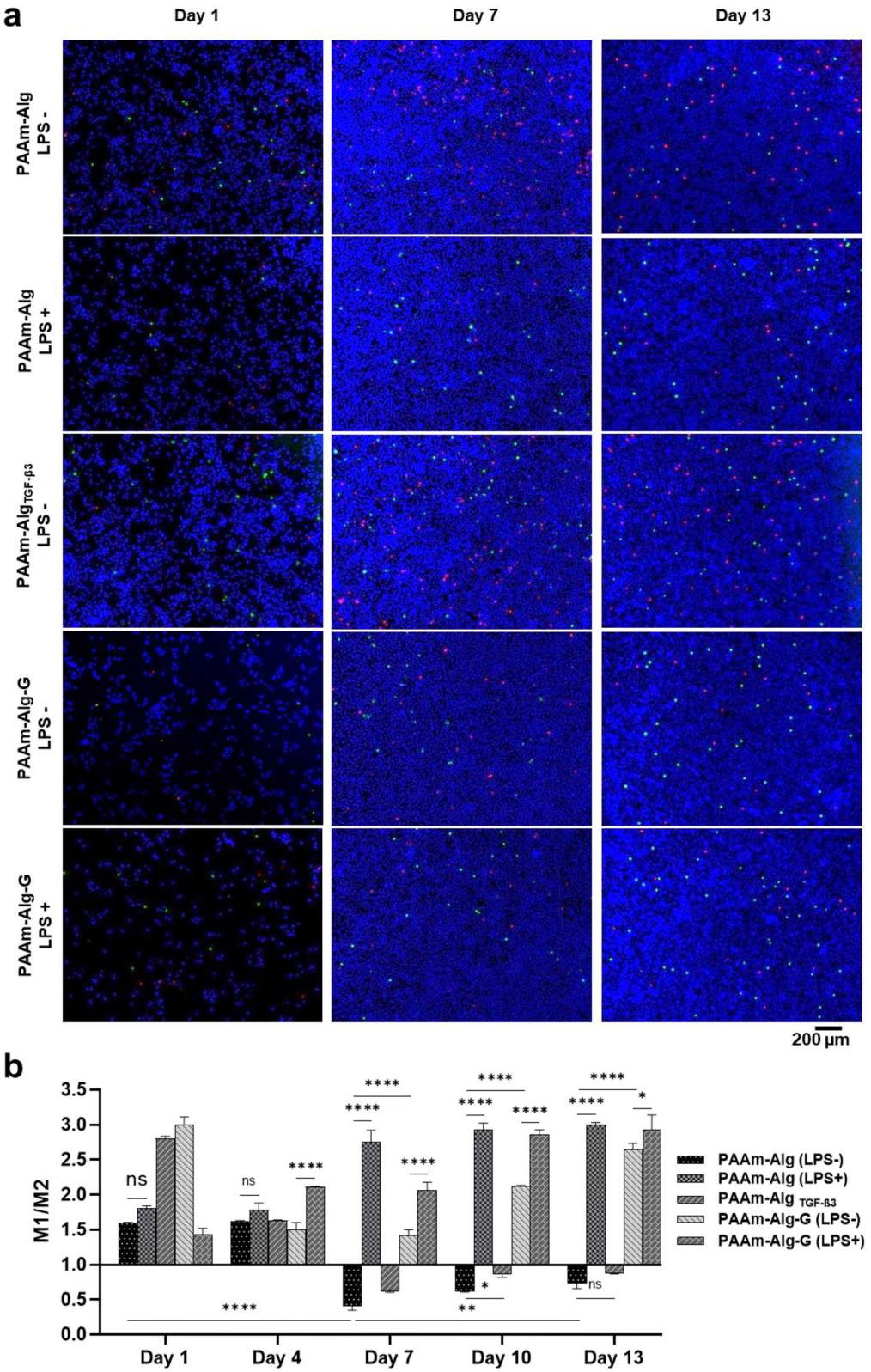

Fig. 4 Evaluation of macrophage polarization. **a** Macrophage polarization over 13 days against hydrogels within the 3D model. Nuclei of ATDC5, L929, and Raw264.7 cells are shown in blue, the M1 surface marker CD80 is green, and the M2 surface marker CD206 is red. **b** M1/M2 ratio induced by hydrogels over 13 days. Two-way ANOVA, Tukey multiple comparison test ($n = 2$ independent experiments). Error bars represent standard deviations (ns: $p > 0.05$, *: $p < 0.05$, **: $p < 0.01$, ****: $p < 0.0001$)

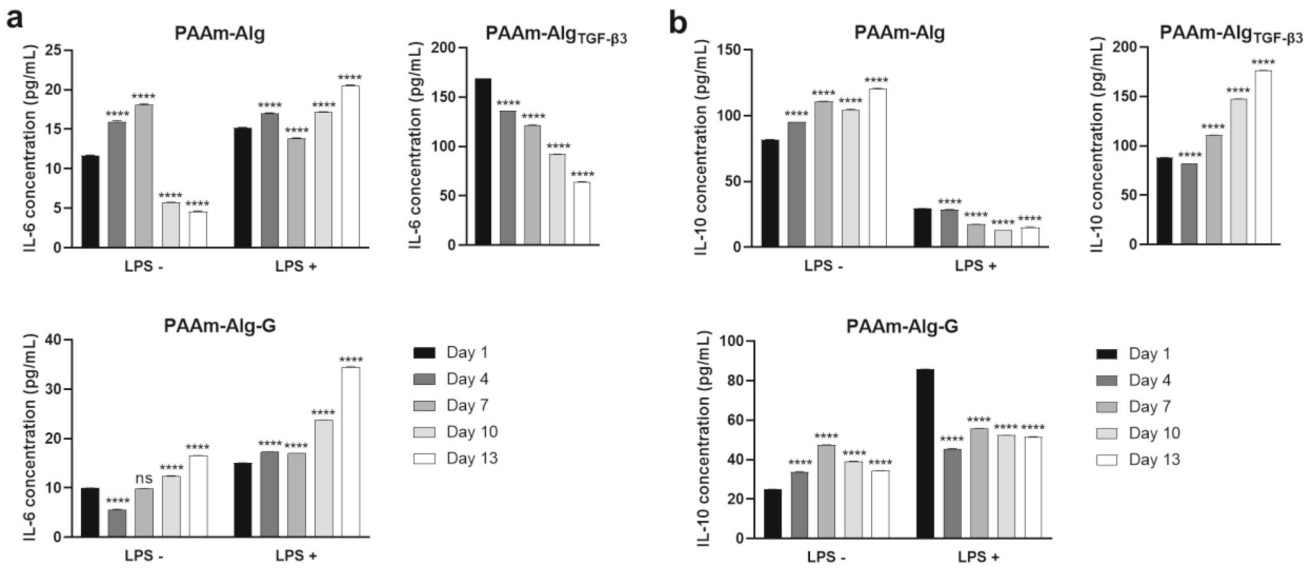

Fig. 5 ELISA results; concentrations of **a** IL-6 and **b** IL-10 cytokines in the supernatant of the 3D model containing PAAm-Alg, PAAm-Alg$_{TGF-\beta3}$, and PAAm-Alg-G hydrogels. Two-way ANOVA, Tukey multiple comparison test ($n = 2$ independent experiments). Error bars represent standard deviations (ns: $p > 0.05$, ****: $p < 0.0001$)

pro-inflammatory and anti-inflammatory effects, depending upon specific immune contexts such as cytokine concentration, treatment time, tissue microenvironment, cellular target, and cytokine synergy [64]. While TGF-β1 and TGF-β2 are associated with fibrotic (scar-forming) healing in adult mammal wounds, TGF-β3 is associated with early regenerative (scar-free) healing in fetal mammal wounds. It induces less COL1A1 and myofibroblast-specific marker ACTA2 transcription, and greater MMP1 [65–67]. Besides its high anti-inflammatory effect, TGF-β3 mediates pro-inflammatory phase in the first stage of the early healing process by releasing high concentrations of inflammatory cytokines such as IL-6. This occurs as a result of the proliferation of immune cells, similar to highly homolog (86%) TGF-β1 [66, 67]. From this point on, treatment time and concentration are the determinants for the pro-inflammatory effects of TGF-β3. In a previous study, when the cytokine profile induced in cervical epithelial cells by TGF-β3 was examined with Luminex microbead and ELISA analysis, researchers noted an up-to-13-fold increase in IL-6 concentration (pg/10^5 cells, after incubation for 12 h, with supernatants collected at 24 h) with increasing TGF-β3 concentrations (0.5, 5, 50 ng/mL), compared to the untreated control; they also found other TGF-β isoforms [68]. The high IL-6 level of the pro-inflammatory response in the first days of the early scar-free healing process induced by TGF-β3 should not be perceived negatively, as this can be associated with chondrocyte proliferation and differentiation in 3D culture, as well as with immune response [69]. We found that in the inflammatory response to PAAm-Alg$_{TGF-\beta3}$ hydrogel, the maximum IL-6 level (168.89 pg/mL) was reached within the first 24 h ($p < 0.0001$). During the following 13 days, IL-6 levels (168.89, 136.25, 121.97, 92.24, and 64.34 pg/mL) decreased, whereas IL-10 levels (88.37, 82.10, 110.77, 147.58 and 176.52 pg/mL) increased ($p < 0.0001$).

As for the PAAm-Alg hydrogel, a significant decrease ($p < 0.0001$) in IL-6 concentration (from 18.12 pg/mL to 4.58 pg/mL) was observed from day 7 to day 13. These data suggested that the transition to the anti-inflammatory phase was achieved, and the healing process started, at the end of day 7. In our previous study, new surface tissue (69.99% and 72.45%) and new cartilage tissue (77.77% and 81.48%) were formed by an in vivo cartilage defect model after implantation of PAAm-Alg and PAAm-Alg$_{TGF-\beta3}$ hydrogels, respectively [26]. The increased IL-10 concentration at the implantation site of the biomaterial reduces the expression of pro-inflammatory cytokines and inhibits proliferation of macrophages, thus suppressing the immune response induced by the biomaterial [70]. Indeed, a significant increase ($p < 0.0001$) in IL-10 was noted at day 13, which was even enhanced from 120.73 pg/mL in PAAm-Alg hydrogel to 176.52 pg/mL in PAAm-Alg$_{TGF-\beta3}$ (Fig. 5b). On the other hand, IL-6 concentration increased for 13 days in LPS + for both hydrogel types, while IL-10 concentration decreased ($p < 0.0001$). In addition to macrophages, pro-inflammatory conditions stimulate the secretion of more IL-6 from chondrocytes in articular cartilage, promoting greater cellular crosstalk with fibroblasts and leading to higher secre-

tion of IL-6 into the synovial fluid [71]. IL-6 was also secreted continuously against PAAm-Alg-G hydrogel for 13 days in LPS–. This was consistent with the results of macrophage analysis, which showed dominant M1 polarization, whereas secretion of IL-10 was 3.5-fold lower than in PAAm-Alg hydrogel. Pro-inflammatory cytokine IL-6 secretion against PAAm-Alg-G hydrogel was expected to increase over 13 days, while the anti-inflammatory cytokine IL-10 was expected to decrease. However, the concentration of IL-10 secreted against PAAm-Alg-G hydrogel was higher in LPS + than in LPS– or PAAm-Alg LPS + . Uncomplicated M1 macrophages produce the pro-inflammatory cytokines IL-6, TNF-α, and IL-1β, while M2 macrophages are divided into four subtypes, M2a, M2b, M2c, and M2d, and also secrete a wider variety of cytokines [72]. The M2d phenotype involved in tumor growth and angiogenesis is not relevant to this study. M2a macrophages, often defined as alternatively activated wound-healing macrophages, secrete important factors for tissue repair, and M2c macrophages (also known as acquired deactivation macrophages) contribute to tissue repair and exhibit potent anti-inflammatory activity [73]. Interestingly, M2b regulatory macrophages are predominantly involved in prolonged or chronic inflammation scenarios [74]. Unlike M2a and M2c macrophages, M2b macrophages, which do not produce an ECM, have the capacity to secrete both pro-inflammatory cytokines such as IL-6, TNF-α, and IL-1β, and anti-inflammatory cytokines such as IL-10. The mannose-receptor CD206 is expressed on M2a and M2c macrophage surfaces, but not on M2b macrophages [75]. In addition, M2b is induced by LPS, unlike the M2a and M2c subtypes of M2 macrophages [76]. Clearly, M2b is biochemically and functionally different from M2a–M2c macrophages. The increase in both IL-6 and IL-10 concentrations in LPS + and LPS– against PAAm-Alg-G hydrogel suggested the presence of M2b macrophages. In addition, higher concentrations of IL-6 and IL-10 were obtained in LPS + compared to LPS–, which is consistent with the knowledge that M2b was stimulated by LPS. Despite high secretion of IL-10, the absence of the CD206 marker indicated the presence of M2b regulatory macrophages, but not of M2a and M2c macrophages that would promote wound healing. Novak et al. found that during the process of tissue repair, the amount of IL-6 decreased, whereas the amount of CD206 increased [77]. Likewise, in the time-dependent immune response results of the current study, we observed a decrease in IL-6 and an increase in CD206 for PAAm-Alg and PAAm-Alg$_{TGF\text{-}\beta3}$ hydrogels. Overall, the developed 3D model was suitable for predicting immune responses to various biomaterials. Unlike the non-biocompatible PAAm-Alg-G hydrogel, both PAAm-Alg and PAAm-Alg$_{TGF\text{-}\beta3}$ hydrogels promoted healing; thus, the utilization of these hydrogels in future clinical studies may reveal promising results.

Conclusions

In this study, GelMA-MeHA provided a favorable environment for culturing chondrocytes, fibroblasts, and macrophages to mimic cellular heterogeneity and allow assessment of immune responses to implantable hydrogels in our 3D in vitro model. The results showed that TGF-β3 loading polarized the immune response against PAAm-Alg hydrogel to a more balanced M1/M2 ratio. The addition of graphite (which has been shown to be toxic to cells) to the hydrogel polarized the macrophages to a predominantly M1 profile and provided a pro-inflammatory environment that compromised tissue healing, as did the use of LPS. By testing both biocompatible and non-biocompatible hydrogels, we were able to validate our 3D in vitro model, and we believe it may serve as an alternative to animal experiments by recapitulating in vivo inflammatory states and permitting immune responses to biomaterials to be readily tested in preclinical studies.

Supplementary Information The online version contains supplementary material available at https://doi.org/10.1007/s42242-022-00198-z.

Acknowledgements This work was supported by the Scientific and Technological Research Council of Turkey (TUBITAK) under the grant number 219M057. PSM acknowledges TUBITAK 2211-A National Graduate Scholarship Program and BC acknowledges TUBITAK 2210-C National Priority Areas Graduate Scholarship Program. YSZ acknowledges support by the Brigham Research Institute.

Author contributions BC, GB, and PSM performed the experiments, collected the data, conducted the data analysis and interpretation, and wrote the manuscript. OYC generated the concept, and designed the study. YSZ and OYC supported the study, involved in writing and critical editing and proofreading the manuscript.

Declarations

Conflict of interest The authors declare that there is no conflict of interest.

Ethical approval Ethical approval is not applicable in this study.

References

1. Shokri A, Ramezani K, Jamalpour MR et al (2022) In vivo efficacy of 3D-printed elastin–gelatin–hyaluronic acid scaffolds for regeneration of nasal septal cartilage defects. J Biomed Mater Res - Part B Appl Biomater 110(3):614–624. https://doi.org/10.1002/jbm.b.34940
2. Alvarez Echazú M, Renou S, Alvarez G et al (2022) A collagen-silica-based biocomposite for potential application in bone tissue engineering. J Biomed Mater Res - Part A 110(2):331–340. https://doi.org/10.1002/jbm.a.37291
3. Gobbi SJ (2019) Requirements for selection/development of a biomaterial. Biomed J Sci Tech Res 14(3):10674–10679. https://doi.org/10.26717/bjstr.2019.14.002554

4. Da Silva K, Kumar P, Choonara YE et al (2020) Three-dimensional printing of extracellular matrix (ECM)-mimicking scaffolds: a critical review of the current ECM materials. J Biomed Mater Res - Part A 108(12):2324–2350. https://doi.org/10.1002/jbm.a.36981
5. Zhang YS, Khademhosseini A (2017) Advances in engineering hydrogels. Science 356(6337):3627. https://doi.org/10.1126/science.aaf3627
6. Mariani E, Lisignoli G, Borzì RM et al (2019) Biomaterials: foreign bodies or tuners for the immune response? Int J Mol Sci 20(3):636. https://doi.org/10.3390/ijms20030636
7. Higgins DM, Basaraba RJ, Hohnbaum AC et al (2009) Localized immunosuppressive environment in the foreign body response to implanted biomaterials. Am J Pathol 175(1):161–170. https://doi.org/10.2353/ajpath.2009.080962
8. Josyula A, Parikh KS, Pitha I et al (2021) Engineering biomaterials to prevent post-operative infection and fibrosis. Drug Deliv Transl Res 11:1675–1688. https://doi.org/10.1007/s13346-021-00955-0
9. Anderson JM, Rodriguez A, Chang DT (2008) Foreign body reaction to biomaterials. Semin Immunol 20(2):86–100. https://doi.org/10.1016/j.smim.2007.11.004
10. Carnicer-Lombarte A, Chen ST, Malliaras GG et al (2021) Foreign body reaction to ımplanted biomaterials and ıts ımpact in nerve neuroprosthetics. Front Bioeng Biotechnol 9:1–22. https://doi.org/10.3389/fbioe.2021.622524
11. Yang X, Liu H, Ye T et al (2020) AhR activation attenuates calcium oxalate nephrocalcinosis by diminishing M1 macrophage polarization and promoting M2 macrophage polarization. Theranostics 10(26):12011–12025. https://doi.org/10.7150/thno.51144
12. Ibáñez-Fonseca A, Maniega SS, del Blanco DG et al (2020) Elastin-like recombinamer hydrogels for ımproved skeletal muscle healing through modulation of macrophage polarization. Front Bioeng Biotechnol 8:1–12. https://doi.org/10.3389/fbioe.2020.00413
13. Krzyszczyk P, Schloss R, Palmer A et al (2018) The role of macrophages in acute and chronic wound healing and interventions to promote pro-wound healing phenotypes. Front Physiol 9:1–22. https://doi.org/10.3389/fphys.2018.00419
14. Filiz Y, Saglam-Metiner P, Ersoy S et al (2022) Supercritical carbon dioxide dried double layer laponite XLS and alginate/polyacrylamide construct and immune response. Tissue Cell 74:101712. https://doi.org/10.1016/j.tice.2021.101712
15. Fishman JM, Wiles K, Wood KJ (2015) The acquired ımmune system response to biomaterials, ıncluding both naturally occurring and synthetic biomaterials. Host Response to Biomaterials: The Impact of Host Response on Biomaterial Selection. Elsevier Inc p.151–187. https://doi.org/10.1016/B978-0-12-800196-7.00008-6
16. Ungemach M, Doll T, Vrana NE (2019) How to predict adverse ımmune reactions to ımplantable biomaterials? Development of an integrated biomaterial risk assessment testing system. Eur J Immunol 49(4):517–520. https://doi.org/10.1002/eji.201970045
17. Wolf MT, Vodovotz Y, Tottey S et al (2015) Predicting in vivo responses to biomaterials via combined in vitro and in silico analysis. Tissue Eng - Part C Methods 21(2):148–159. https://doi.org/10.1089/ten.tec.2014.0167
18. Sharifi F, Htwe SS, Righi M et al (2019) A foreign body response-on-a-chip platform. Adv Healthc Mater 8(4):1–10. https://doi.org/10.1002/adhm.201801425
19. Shen T, Dai K, Yu Y et al (2020) Sulfated chitosan rescues dysfunctional macrophages and accelerates wound healing in diabetic mice. Acta Biomater 117:192–203. https://doi.org/10.1016/j.actbio.2020.09.035
20. Saleh LS, Bryant SJ (2017) In vitro and in vivo models for assessing the host response to biomaterials. Drug Discov Today Dis Model 24:13–21. https://doi.org/10.1016/j.ddmod.2018.04.002
21. McNally AK, Anderson JM (2015) Phenotypic expression in human monocyte-derived interleukin-4-induced foreign body giant cells and macrophages in vitro: dependence on material surface properties. J Biomed Mater Res Part A 103(4):1380–1390. https://doi.org/10.1002/jbm.a.35280
22. Damanik FF, Rothuizen TC, van Blitterswijk C et al (2014) Towards an in vitro model mimicking the foreign body response: tailoring the surface properties of biomaterials to modulate extracellular matrix. Sci Rep 4(1):1–11. https://doi.org/10.1038/srep06325
23. Patel DK, Dutta SD, Hexiu J et al (2022) 3D-printable chitosan/silk fibroin/cellulose nanoparticle scaffolds for bone regeneration via M2 macrophage polarization. Carbohyd Polym 281:119077. https://doi.org/10.1016/j.carbpol.2021.119077
24. Park Y, Huh KM, Kang SW (2021) Applications of biomaterials in 3D cell culture and contributions of 3D cell culture to drug development and basic biomedical research. Int J Molec Sc 22(5):2491. https://doi.org/10.3390/ijms22052491
25. Antoni D, Burckel H, Josset E et al (2015) Three-dimensional cell culture: a breakthrough in vivo. Int J Molec Sci 16(3):5517–5527. https://doi.org/10.3390/ijms16035517
26. Saygili E, Kaya E, Ilhan-Ayisigi E et al (2021) An alginate-poly(acrylamide) hydrogel with TGF-β3 loaded nanoparticles for cartilage repair: biodegradability, biocompatibility and protein adsorption. Int J Biol Macromol 172:381–393. https://doi.org/10.1016/j.ijbiomac.2021.01.069
27. Jansen T, Wallin RF (1998) A practical guide to ISO 10993–12: sample preparation and reference materials. Med Dev Diagnos Ind 20:61–62
28. Yue K, Li X, Schrobback K et al (2017) Structural analysis of photocrosslinkable methacryloyl-modified protein derivatives. Biomaterials 139:163–171. https://doi.org/10.1016/j.biomaterials.2017.04.05029
29. Cebe T, Ahuja N, Monte F et al (2020) Novel 3D-printed methacrylated chitosan-laponite nanosilicate composite scaffolds enhance cell growth and biomineral formation in MC3T3 pre-osteoblasts. J Mater Res 35(1):58–75. https://doi.org/10.1557/jmr.2018.260
30. Xu M, Ma D, Chen D et al (2018) Preparation, characterization and application research of a sustained dexamethasone releasing electrode coating for cochlear implantation. Mater Sci Eng C 90:16–26. https://doi.org/10.1016/j.msec.2018.04.033
31. Tsanaktsidou E, Kammona O, Kiparissides C (2019) On the synthesis and characterization of biofunctional hyaluronic acid based injectable hydrogels for the repair of cartilage lesions. Eur Polym J 114:47–56. https://doi.org/10.1016/j.eurpolymj.2019.02.024
32. Negrescu AM, Necula MG, Gebaur A et al (2021) In vitro macrophage immunomodulation by poly(ε-caprolactone) based-coated AZ31 Mg Alloy. Int J Mol Sci 22(2):1–36. https://doi.org/10.3390/ijms22020909
33. Liu L, Li X, Shi X et al (2018) Injectable alendronate-functionalized GelMA hydrogels for mineralization and osteogenesis. RSC Adv 8(40):22764–22776. https://doi.org/10.1039/C8RA03550D
34. Benatti ACB, Xavier MV, Macedo MF et al (2016) Comparative analysis of biocompatibility between Poly (Llactic Acid) (PLLA) and PLDL Purac® nanofibers for use in tissue engineering. Chem Eng Trans 49:199–204
35. Pereira I, Fraga S, Silva S et al (2019) In vitro genotoxicity assessment of an oxidized dextrin-based hydrogel for biomedical applications. J Appl Toxicol 39(4):639–649. https://doi.org/10.1002/jat.3754
36. Wang X, Harrison JS, Studzinski GP (2016) Enhancement of arabinocytosine (AraC) toxicity to AML cells by a differentiation agent combination. J Steroid Biochem Mol Biol 164:72–78. https://doi.org/10.1016/j.jsbmb.2015.08.023

37. Lam T, Dehne T, Krüger JP et al (2019) Photopolymerizable gelatin and hyaluronic acid for stereolithographic 3D bioprinting of tissue-engineered cartilage. J Biomed Mater Res 107(8):2649–2657. https://doi.org/10.1002/jbm.b.34354
38. Montoya C, Du Y, Gianforcaro AL et al (2021) On the road to smart biomaterials for bone research: definitions, concepts, advances, and outlook. Bone Res 9(1):12. https://doi.org/10.1038/s41413-020-00131-z
39. Ospelt C (2017) Synovial fibroblasts in 2017. RMD Open 3(2):1–10. https://doi.org/10.1136/rmdopen-2017-000471
40. Arzi B, Duraine GD, Lee CA et al (2015) Cartilage immunoprivilege depends on donor source and lesion location. Acta Biomater 23:72–81. https://doi.org/10.1016/j.actbio.2015.05.025
41. pedron s, hanselman js, schroeder ma, et al (2017) extracellular hyaluronic acid ınfluences the efficacy of EGFR tyrosine kinase ınhibitors in a biomaterial model of glioblastoma. Adv Healthc Mater 6(21):1–9. https://doi.org/10.1002/adhm.201700529
42. Gupta RC, Lall R, Srivastava A et al (2019) Hyaluronic acid: molecular mechanisms and therapeutic trajectory. Front Vet Sci 6:1–24. https://doi.org/10.3389/fvets.2019.00192
43. Fonsi M, El Amrani AI, Gervais F et al (2020) Intra-articular hyaluronic acid and chondroitin sulfate: pharmacokinetic ınvestigation in osteoarthritic rat models. Curr Ther Res 92:100573. https://doi.org/10.1016/j.curtheres.2019.100573
44. Rayahin JE, Gemeinhart RA (2017) Activation of macrophages in response to biomaterials. Results Probl Cell Differ 62:317–351. https://doi.org/10.1007/978-3-319-54090-0_13
45. Laffer B, Bauer D, Wasmuth S et al (2019) Loss of IL-10 promotes differentiation of microglia to a M1 phenotype. Front Cell Neurosci 13:1–12. https://doi.org/10.3389/fncel.2019.00430
46. Zheng Z, Chen Y, Hong H et al (2021) The "Yin and Yang" of ımmunomodulatory magnesium-enriched graphene oxide nanoscrolls decorated biomimetic scaffolds in promoting bone regeneration. Adv Healthc Mater 10(2):1–14. https://doi.org/10.1002/adhm.202000631
47. Zakrzewska KE, Samluk A, Wierzbicki M et al (2015) Analysis of the cytotoxicity of carbon-based nanoparticles, diamond and graphite, in human glioblastoma and hepatoma cell lines. PLoS ONE 10(3):1–15. https://doi.org/10.1371/journal.pone.0122579
48. Rezazadeh Azari M, Mohammadian Y (2020) Comparing in vitro cytotoxicity of graphite, short multi-walled carbon nanotubes, and long multi-walled carbon nanotubes. Environ Sci Pollut Res 27(13):15401–15406. https://doi.org/10.1007/s11356-020-08036-4
49. Chatterjee S (2016) Oxidative stress, ınflammation, and disease: oxidative stress and biomaterials. Elsevier Inc p.35–58 Doi: https://doi.org/10.1016/B978-0-12-803269-5.00002-4
50. Huyer LD, Pascual-Gil S, Wang Y et al (2020) Advanced strategies for modulation of the material–macrophage interface. Adv Funct Mater 30(44):1–21. https://doi.org/10.1002/adfm.201909331
51. Zhou G, Groth T (2018) Host responses to biomaterials and anti-ınflammatory design—a brief review. Macromol Biosci 18(8):1–15. https://doi.org/10.1002/mabi.201800112
52. Bullock CJ, Bussy C (2019) Biocompatibility considerations in the design of graphene biomedical materials. Adv Mater Interf 6(11):1900229. https://doi.org/10.1002/admi.201900229
53. Cha BH, Shin SR, Leijten J et al (2017) Integrin-mediated ınteractions control macrophage polarization in 3D hydrogels. Adv Healthc Mater 6(21):1–12. https://doi.org/10.1002/adhm.201700289
54. Kharaziha M, Baidya A, Annabi N (2021) Rational design of ımmunomodulatory hydrogels for chronic wound healing. J Adv Mater 33(39):2100176. https://doi.org/10.1002/adma.202100176
55. Brown BN, Ratner BD, Goodman SB et al (2012) Macrophage polarization: an opportunity for improved outcomes in biomaterials and regenerative medicine. Biomaterials 33(15):3792–3802. https://doi.org/10.1016/j.biomaterials.2012.02.034
56. Sridharan R, Cavanagh B, Cameron AR et al (2019) Material stiffness influences the polarization state, function and migration mode of macrophages. Acta Biomater 89:47–59. https://doi.org/10.1016/j.actbio.2019.02.048
57. Lebaudy E, Fournel S, Lavalle P et al (2021) Recent advances in antiinflammatory material design. Adv Healthc Mater 10(1):1–20. https://doi.org/10.1002/adhm.202001373
58. Cerqueira A, Araújo-Gomes N, Zhang Y et al (2021) Evaluation of the inflammatory responses to sol–gel coatings with distinct biocompatibility levels. J Biomed Mater Res - Part A 109(9):1539–1548. https://doi.org/10.1002/jbm.a.37149
59. O'Brien EM, Spiller KL (2021) Pro-inflammatory polarization primes macrophages to transition into a distinct M2-like phenotype in response to IL-4. J Leukoc Biol (Early View). https://doi.org/10.1002/Jlb.3a0520-338r
60. Martin KE, García AJ (2021) Macrophage phenotypes in tissue repair and the foreign body response: Implications for biomaterial-based regenerative medicine strategies. Acta Biomater 133:4–16. https://doi.org/10.1016/j.actbio.2021.03.038
61. Gilmour AD, Woolley AJ, Poole-Warren LA et al (2016) A critical review of cell culture strategies for modelling intracortical brain implant material reactions. Biomaterials 91:23–43. https://doi.org/10.1016/j.biomaterials.2016.03.011
62. Anderson J, Cramer S (2015) Perspectives on the Inflammatory, Healing, and Foreign Body Responses to Biomaterials and Medical Devices: Host Response to Biomaterials: The Impact of Host Response on Biomaterial Selection. Elsevier Inc. p.13–36. https://doi.org/10.1016/B978-0-12-800196-7.00002-5
63. Sridharan R, Cameron AR, Kelly DJ et al (2015) Biomaterial based modulation of macrophage polarization: A review and suggested design principles. Mater Today 18(6):313–325. https://doi.org/10.1016/j.mattod.2015.01.019
64. Komai T, Okamura T, Inoue M et al (2018) Reevaluation of pluripotent cytokine TGF-β3 in immunity. Int J Mol Sci 19(8):1–15. https://doi.org/10.3390/ijms19082261
65. Chang Z, Kishimoto Y, Hasan A et al (2014) TGF-β3 modulates the inflammatory environment and reduces scar formation following vocal fold mucosal injury in rats. DMM Dis Model Mech 7(1):83–91. https://doi.org/10.1242/dmm.013326
66. Fujio K, Okamura T, Sumitomo S et al (2016) Therapeutic potential of regulatory cytokines that target B cells. Int Immunol 28(4):189–195. https://doi.org/10.1093/intimm/dxv069
67. Okamura T, Morita K, Iwasaki Y et al (2015) Role of TGF-β3 in the regulation of immune responses. Clin Exp Rheumatol 33:63–69
68. Sharkey DJ, Macpherson AM, Tremellen KP et al (2012) TGF-β mediates proinflammatory seminal fluid signaling in human cervical epithelial cells. J Immunol 189(2):1024–1035. https://doi.org/10.4049/jimmunol.1200005
69. Kondo M, Yamaoka K, Sakata K et al (2015) Contribution of the interleukin-6/STAT-3 signaling pathway to chondrogenic differentiation of human mesenchymal stem cells. Arthritis Rheumatol 67(5):1250–1260. https://doi.org/10.1002/art.39036
70. Zhang B, Su Y, Zhou J et al (2021) Toward a better regeneration through ımplant-mediated ımmunomodulation: harnessing the ımmune responses. Adv Sci 8(16):2100446. https://doi.org/10.1002/advs.202100446
71. Pearson MJ, Herndler-Brandstetter D, Tariq MA et al (2017) IL-6 secretion in osteoarthritis patients is mediated by chondrocyte-synovial fibroblast cross-talk and is enhanced by obesity. Sci Rep 7:3451. https://doi.org/10.1038/s41598-017-03759-w

72. Ollewagen T, Myburgh KH, van de Vyver M et al (2021) Rheumatoid cachexia: the underappreciated role of myoblast, macrophage and fibroblast interplay in the skeletal muscle niche. J Biomed Sci 28:15. https://doi.org/10.1186/s12929-021-00714-w
73. Wang L, xun, Zhang S xi, Wu H juan, et al (2019) M2b macrophage polarization and its roles in diseases. J Leukoc Biol 106(2):345–358. https://doi.org/10.1002/JLb.3ru1018-378rr
74. Klopfleisch R (2016) Macrophage reaction against biomaterials in the mouse model – phenotypes, functions and markers. Acta Biomater 43:3–13. https://doi.org/10.1016/j.actbio.2016.07.003
75. Rőszer T (2015) Understanding the mysterious M2 macrophage through activation markers and effector mechanisms. Mediators Inflamm 2015:816460. https://doi.org/10.1155/2015/816460
76. Novak ML, Koh TJ (2013) Macrophage phenotypes during tissue repair. J Leukoc Biol 93(6):875–881. https://doi.org/10.1189/jlb.1012512
77. Brown BN, Badylak SF (2013) Expanded applications, shifting paradigms and an improved understanding of host-biomaterial interactions. Acta Biomater 9(2):4948–4955. https://doi.org/10.1016/j.actbio.2012.10.025